Transient axial solution for plane and axisymmetric waves focused by a paraboloidal reflector

Yi-Te Tsai and Jinying Zhu[a)]
Department of Civil, Architectural and Environmental Engineering, The University of Texas at Austin, Austin, Texas 78712-1068

Michael R. Haberman
Applied Research Laboratories & The Department of Mechanical Engineering, The University of Texas at Austin, Austin, Texas 78713-8029

(Received 25 October 2012; revised 26 January 2013; accepted 11 February 2013)

A time domain analytical solution is presented to calculate the pressure response along the axis of a paraboloidal reflector for a normally incident plane wave. This work is inspired by Hamilton's axial solution for an ellipsoidal mirror and the same methodology is employed in this paper. Behavior of the reflected waves along reflector axis is studied, and special interest is placed on focusing gain obtained at the focal point. This analytical solution indicates that the focusing gain is affected by reflector geometry and the time derivative of the input signal. In addition, focused pressure response in the focal zone given by various reflector geometries and input frequencies are also investigated. This information is useful for selecting appropriate reflector geometry in a specific working environment to achieve the best signal enhancement. Numerical simulation employing the finite element method is used to validate the analytical solution, and visualize the wave field to provide a better understanding of the propagation of reflected waves. This analytical solution can be modified to apply to non-planar incident waves with axisymmetric wavefront and non-uniform pressure distribution. An example of incident waves with conical-shaped wavefront is presented.
 [http://dx.doi.org/10.1121/1.4794367]

PACS number(s): 43.35.Zc, 43.20.Fn, 43.20.Px, 43.40.Dx [ANN] Pages: 2025–2035

I. INTRODUCTION

Paraboloidal reflectors have been widely used in various fields to collect the energy of sound, light, and radio waves. The unique geometry of a parabola enables a normally incident plane wave traveling along the axis to be focused to the focal point, and the signal strength at the focal point is enhanced consequently. In nondestructive evaluation, the airborne plane waves generated by a planar air-coupled transducer can be focused by a paraboloidal reflector.[1] Recently Dai *et al*.[2] have used a paraboloidal reflector to amplify the airborne zero-group-velocity Lamb wave signals radiated from a concrete plate and to improve the signal to noise ratio. The S1 zero-group-velocity (S1ZGV) Lamb wave mode has been found to show high excitability and allow high transmission efficiency of acoustic waves through plates.[3] The S1ZGV theory also provides theoretical explanation to the impact-echo testing, a common non-destructive testing (NDT) method for concrete structures.[4] The feasibility of air-coupled impact-echo testing has been validated on concrete specimens in laboratory[5] and field testing.[6] Numerical simulations by Tsai *et al*.[7] showed that the airborne S1ZGV mode wave radiated from a plate can be regarded as a quasi-plane wave with a small radiation angle (conical wavefront), which can be effectively focused by a paraboloidal reflector. The signal amplification owning to focusing depends on geometry of a paraboloidal reflector. Therefore, it is essential to understand the behavior of the reflected waves and the focusing effect caused by a paraboloidal reflector.

Acoustical properties of a paraboloidal reflector have long been investigated.[8–11] Wahlstrom[12] studied the on-axis pressure response of paraboloidal reflectors and the signal amplification at the focal point. Wahlstrom used the velocity potential to derive a solution for incident harmonic plane waves, and studied the dependence of signal amplification at focus on reflector geometry and the input frequency. Cornet and Blackstock[13] developed a theoretical solution for a spherical reflector with an incident spherical N wave generated by a spark source located on the reflector axis. This solution employs the Kirchhoff-Helmholtz (K-H) integral theorem to obtain the reflected response along the reflector axis. Hamilton[14] further extended their solution and derived a transient axial solution for an ellipsoidal reflector with a spark source located at the near focus. Geometrical acoustics was used to describe the initial condition on reflector surface. Hamilton[15] and Gelin[16] later also investigated reflection of a spherical wave from a paraboloidal mirror analytically and experimentally.

In this paper the authors employ the same analysis procedure used in Hamilton's work[14] to obtain the transient pressure response along the axis of a paraboloidal reflector for a normally incident plane wave. This paper includes four major components. First, the axial pressure response obtained using geometrical acoustics and K-H integral is presented, and the behavior of the reflected waves is

[a)]Author to whom correspondence should be addressed. Electronic mail: jyzhu@mail.utexas.edu

discussed. Second, on-axis pressure responses obtained from numerical simulations are presented for comparison, and the wave field is visualized using numerical simulation results. Third, signal amplification at the focal point and the size of focal zone are investigated for reflectors with various geometries and incident plane waves with different frequencies. Finally, the authors show the potential application of this solution to incident waves with axisymmetric wavefront and non-uniform pressure distribution. An incident wave with a conical-shaped wavefront is presented as an example.

II. METHODOLOGY

The analytical solution presented in this paper calculates the time-domain pressure response along the axis of a paraboloidal reflector for a normally incident plane wave. The method in Hamilton's work[14] based on geometrical acoustics and the K-H integral is employed. The pressure distribution over the reflector surface is first obtained by geometrical acoustics. The axial response of the reflected and diffracted wave field is then calculated using the K-H integral, which can be used to find pressure at any point in an enclosed surface if the pressure on the surface is specified.

Figure 1 shows the model of a paraboloidal reflector and a source plane that radiates plane waves. The geometry of paraboloidal reflector is described by the equation $r^2 = 4z_F z$, where z_F is the focal length (distance between reflector vertex and focal point). The variable h represents the depth of the reflector and h_v is the distance between the vertex and the source plane. The symbol z_s denotes the z coordinate of any point on the reflector surface and r_F represents the distance between that surface point and the focal point. These two variables have the relation of $r_F = z_F + z_s$ according to the geometric property of a parabola. For an incident plane wave with amplitude of p_0, p_1 represents the wave pressure on the reflector surface, and p_{2g} denotes the reflected pressure in space at a distance r_2 from the focal point, where the subscript "g" represents geometrical acoustic estimation. Figure 1 shows two observation points located along the reflector axis. Point A is located "before" the focal point and point B is "beyond" the focal point. The distance between an observation point and any point on the reflector surface is defined by R.

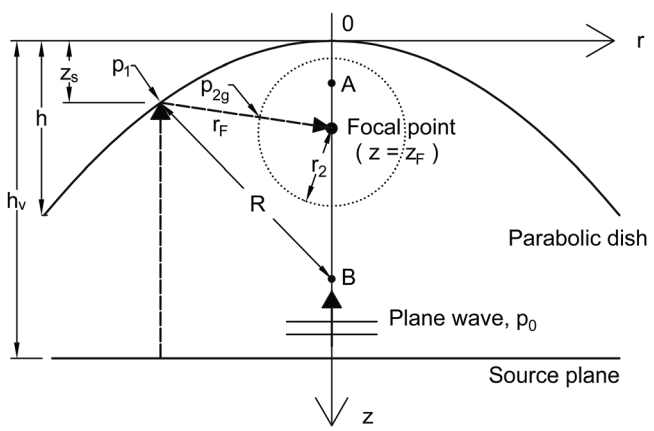

FIG. 1. Layout of paraboloidal reflector and source plane that radiates plane waves with a peak amplitude of p_0. The dashed line shows any ray parallel to the reflector axis passes through the focal point after reflection.

A. Geometrical acoustics

As shown in Fig. 1, the source plane generates plane waves with sizes large enough to cover the entire reflector aperture. When the plane wave reaches the reflector surface, the reflector will focus waves to the focal point. Geometrical acoustics is valid for $ka \gg 1$, where k is the wavenumber of the lowest frequency of incident wave, and a is the minimum radius of curvature of the paraboloidal reflector.[17] Within the frame work of geometrical acoustics, the incident sound waves are represented as a group of rays. Geometrical acoustics is employed to determine the pressure amplitude at any point along the ray path, and to calculate the travel time of a sound wave.

The reflected pressure along the ray path is estimated as follows. First, under the assumption that the pressure amplitude of the incident plane wave does not change until it reaches reflector plane, the incident pressure on the surface (p_1 in Fig. 1) has an amplitude of p_0. By assuming the reflection coefficient at the reflector−air interface as 1, the reflected pressure amplitude equals to p_0 as well. Therefore, the reflected pressure on the reflector surface is described as

$$p_1(t, z_s) = p_0 f\left(t - \frac{h_v - z_s}{c_0}\right), \tag{1}$$

where c_0 is the sound speed, and $f(t)$ is a dimensionless function describing the input function.

Since all rays reflected from the reflector surface converge to the focus at the same time, the relation between the reflected pressure (p_{2g}) and the pressure on the reflector surface (p_1) along these reflected rays can be obtained by considering the focus as a center of an imaginary converging spherical wave. As a result, the amplitude of p_{2g} obtained at a distance r_2 from the focal point can be described by $|p_{2g}|r_2 = |p_1|r_F$ for each ray. Combining this pressure relation with Eq. (1), the reflected pressure field can be written as

$$\frac{p_{2g}}{p_0} = \frac{r_F}{r_2} f\left(t - \frac{h_v + z_F - r_2}{c_0}\right), \tag{2}$$

where $(h_v + z_F - r_2)/c_0$ is the time required for a sound ray to travel from the source plane to a point located on the ray path at a distance r_2 from focus.

Equation (2) gives spatial and temporal information for the reflected pressure field using geometrical acoustics and describes the contribution from any point on the reflector surface. Note that the effect of diffraction is not considered in the geometrical acoustics analysis.

B. Kirchhoff-Helmholtz integral

The K-H integral can be used to calculate the pressure response at a point enclosed by a closed surface when the initial condition is known.[18] Here the K-H integral is employed to calculate the reflected pressure response along

the reflector axis which accounts for diffraction. The initial condition (the pressure on the reflector surface and its inward normal derivative) is described by geometrical acoustics using Eq. (2). Given the pressure on the reflector surface resulting from an incident plane wave, the transient model resulting from the evaluation of the K-H integral is provided in Eqs. (4)–(11) of this section. The details of the model derivation are important and non-trivial but can obfuscate the relevant physical details of the results. Therefore, this section provides the model and a discussion of the components while the full derivation is provided in Appendix A.

The reflected pressure p_2 is calculated by the K-H integral as

$$p_2 = \frac{1}{4\pi}\int\int_S \left\{ [p_{2g}]\frac{\partial}{\partial n}\left(\frac{1}{R}\right) - \frac{1}{c_0 R}\frac{\partial R}{\partial n}\left[\frac{\partial p_{2g}}{\partial t}\right] - \frac{1}{R}\left[\frac{\partial p_{2g}}{\partial n}\right]\right\} ds, \tag{3}$$

where $\partial/\partial n$ is the derivative in the inward direction normal to the reflector surface, and the brackets $[\cdot]$ indicate that any time related argument presented inside the bracket is delayed by R/c_0.[18]

In Eq. (3), the K-H integral integrates over the entire closed surface, which is not the case for a paraboloidal reflector because its surface ends at the aperture. However, since the reflected rays only come from the reflector surface, all contributions of p_{2g} and its normal derivative from outside the reflector aperture must be zero. Therefore, only part of the integral gives a non-zero value. The pressure p_2 along the reflector axis can therefore be written as

$$\frac{p_2}{p_0} = H_e(z)f(\tau_e) + H_c(z)f(\tau_c) + \int_{t_1}^{t_2} H_w(z,t')f(t-t')dt', \tag{4}$$

where H_e, H_c, and H_w are scaling factors for different reflected waves, τ is the retarded time, and z is the vertical location of the observation point. The limits of integration t_1 and t_2 correspond to the arrival times of the first and last arrived wave, respectively.

On the right hand side of Eq. (4), the first two terms correspond to the two limits (edge and center) in the K-H integral, and the last term is the contribution from the entire surface. The first term is the edge wave representing contributions to the on-axis field resulting from the edge diffraction. The second term is the center wave,[14] which represents the reflected wave from the reflector vertex. The third term is known as the wake,[19] which is due to non-uniform pressure distribution on the surface. As indicated in Eq. (4), both the center and edge waves have the same waveform as the input wave but with different arrival times and scaling factors. The integral indicates that the wake is superposition of waves reflected from the entire surface. The pressure amplitude and phase of each type of reflected waves are determined by the corresponding scaling factors, which are functions of the observation location z. The functions in Eq. (4) are defined as

$$H_e(z) = \frac{z_F(z+h+R_e)}{R_e K_e}, \tag{5}$$

$$H_c(z) = -\frac{z_F(z+R_c)}{R_c K_c}, \tag{6}$$

$$H_w(z,t') = -\frac{z_F c_0 (z+z_r+R_r)\mathrm{sgn}(K_r)}{(z_r+z_F)K_r^2}, \tag{7}$$

$$R = \sqrt{4z_F z_s + (z-z_s)^2}, \tag{8}$$

$$K_{e,c,r} = R_{e,c,r} + z - z_s - 2z_F, \tag{9}$$

$$\tau = t - \frac{h_v - z_s + R}{c_0}, \tag{10}$$

and

$$z_r = \frac{(t'c_0 - h_v)^2 - z^2}{4z_F - 2(t'c_0 - h_v + z)}. \tag{11}$$

In these expressions, the subscripts e, c, r indicate that the functions R, K, τ are evaluated at $z_s = h$ (edge), $z_s = 0$ (center), and $z_s = z_r$, respectively, where z_r is the root of $\tau(z_s) = 0$. The sign of K is positive for $z > z_F$ (beyond the focus), and negative for $z < z_F$ (before the focus).

III. ON-AXIS PRESSURE RESPONSE

A. Reflected pressure response along axis for an incident plane wave

Figure 2(a) shows an example of the reflected on-axis pressure response calculated from a point 3 cm before the focal point. For this example, the paraboloidal reflector has a radius of 10 cm and a depth of 5 cm, and the focal point is located at $z = 5$ cm. The distance between reflector vertex and source plane (h_v) is 30 cm. A single cycle sinusoidal wave with a period of 50 μs is used as input. The direct wave (incident wave) is also shown for reference. In this figure, the three components (edge, center and wake) of the reflected field are distinctly observed. Since the observation point is located between the focal point and the reflector vertex, the travel distance for the center wave to reach the observation point is shorter than that for edge wave. As a result, the center wave arrives earlier than the edge wave. Since the wake is reflected from the entire surface between the center and the edge of the reflector, arrival time of the wake spans between that of center wave and edge wave.

The center and edge waves in Fig. 2(a) have similar waveforms as the input function but different amplitudes and phases, respectively. The wake is formed by superposition of many surface-reflected waves that have similar waveform but different time delays, as indicated in Eq. (4). Compared to the direct wave, the phase of edge wave is inverted while the phase of center wave stays the same as input function. This phase difference is related to the location of observation point. Since the observation point is located between the focal point and reflector vertex, the edge wave changes sign when it passes through the focal point.

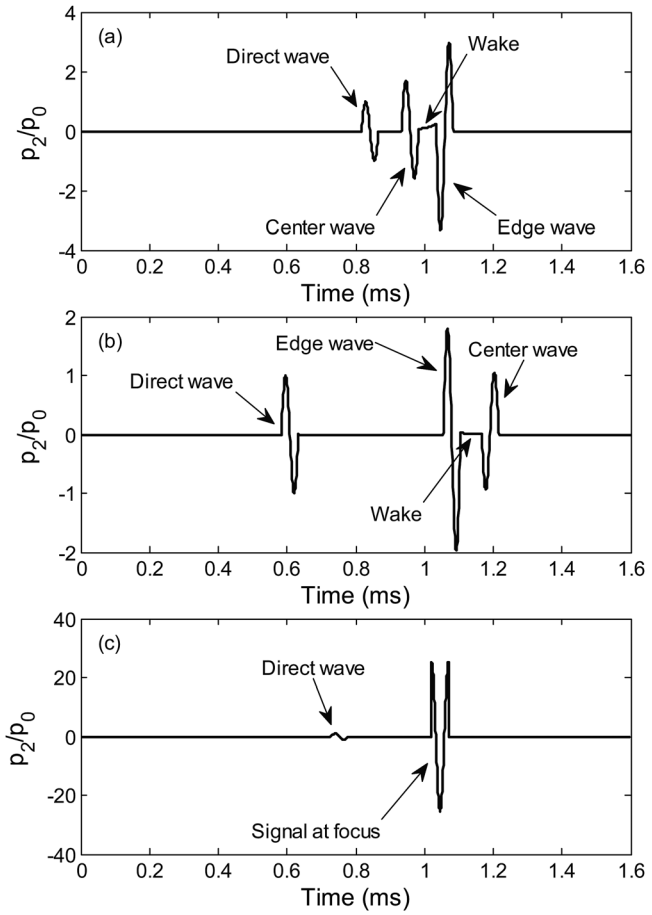

FIG. 2. On-axis time-domain signals at (a) 3 cm before focus ($z = 2$ cm), (b) 5 cm beyond focus ($z = 10$ cm), and (c) focus ($z = 5$ cm). The edge wave in (a) and the center wave in (b) have inversed phase compared to the input signal. The waveform at the focus is the derivative of the input function.

Figure 2(b) shows the axial time-domain signal obtained at 5 cm beyond the focal point. Since the travel distance for the center wave to reach the observation point is longer than that for the edge wave, the edge wave arrives first, followed by the wake and the center wave. Comparing to this figure to Fig. 2(a), both the center and edge waves change phases. Because the observation point is now located beyond the focal point, the center wave passes through focal point (changes from converging to diverging) and changes sign. The wake also changes sign as indicated in Eq. (7).

B. Response at focus with plane wave incident

Figure 2(c) shows the focused pressure response at the focal point. Due to singularity of function K in Eqs. (5)–(7) at $z = z_F$, the pressure at the focal point must be obtained separately. The procedure is presented in Appendix B. After substituting $z = z_F$ into Eq. (A13) and convolving the impulse response with the input function, $f(t)$, the focused pressure response can be written as

$$\frac{p_2}{p_0} = \frac{2z_F \ln(h/z_F + 1)}{c_0} \frac{d}{dt} f\left(t - \frac{h + z_F}{c_0}\right), \tag{12}$$

where h is the depth of reflector. Eq. (12) indicates that the pressure waveform at the focus has a shape of the derivative of the input function, which is shown in Fig. 2(c). Note that the signal gain factor is determined by geometry of the paraboloidal reflector and the frequency contents of the incident wave. Detailed analysis of that observation is presented in Sec. V.

IV. NUMERICAL VERIFICATION

A. Numerical analysis: Model description

In this section, the on-axis analytical solution for a paraboloidal reflector is validated by numerical simulation using the finite element method (FEM) in ABAQUS/Explicit with a 2D axisymmetric model. ABAQUS/Explicit utilizes the explicit Newmark scheme, which employs the central difference method for direct time integration and is widely used for simulating elastic wave propagation problems.[20] Figure 3(a) shows the model used to simulate an airborne incident plane wave and the paraboloidal reflector. The 2D axisymmetric model consists of two domains: an aluminum paraboloidal reflector and an air section. Properties of air are $\rho = 1.21$ kg/m^3, $c_0 = 343$ m/s, and those of the aluminum reflector are $\rho = 2700$ kg/m^3, $E = 71$ GPa, and $\nu = 0.33$. The dimension used in the air domain is 30 cm by 30 cm to simulate a cylinder of air having a radius of 30 cm and a height of 30 cm. The vertex of the aluminum paraboloidal reflector is 20 cm above the bottom boundary of the air section. The reflector has a thickness of 2 mm and a radius of 8 cm. The focal point is located 3.1 cm from reflector vertex. The air and aluminum reflector domains are simulated as having a perfect fluid−solid interaction by assuming continuity of pressure and normal displacement across their interface. A single cycle sinusoidal wave [Fig. 3(b)] with a period of T is used as an input function and is specified over the bottom surface (source plane) of the air domain.

The mesh size used in the air section is selected based on the wavelength of the airborne wave. To properly simulate a propagating wave, a mesh size smaller than 1/10 of the smallest wavelength is required. This criterion indicates the propagating wave should be described by more than 10 nodes.[21–23] The smallest wavelength in air is 17 mm for T = 50 μs. To insure accurate results, a mesh size of 0.5 mm

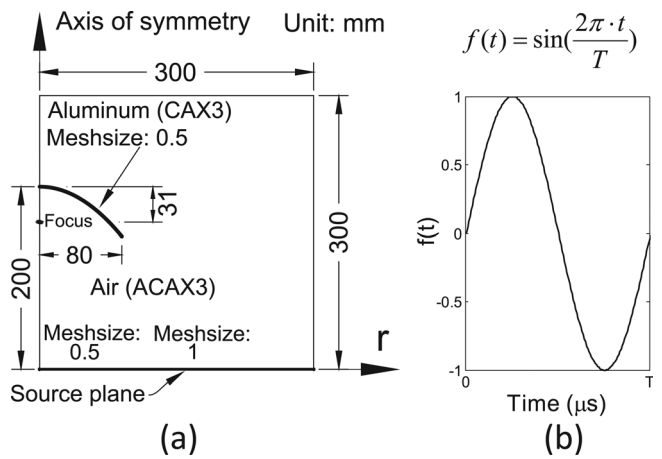

FIG. 3. (a) Model used in ABAQUS for FEM simulation, (b) input function as a single-cycle sinusoid with a duration of T.

($\lambda/34$) was used for the air domain. The mesh size used in the aluminum reflector is 0.5 mm to match the nodes in the air section. Triangular linear axisymmetric acoustic elements (ACAX3) were used in the air section, and triangular linear axisymmetric solid elements (CAX3) were used in the paraboloidal reflector.

B. FEM analysis: Simulation results

1. Wave field visualization

Four snapshot pictures for the wave fields in air obtained at different times are shown in Fig. 4 for a single cycle sinusoidal pulse with duration of 50 μs. Note that the FEM model is 2D axisymmetric, and each image shown in Fig. 4 consists of an original image (right-half) and its mirror image (left-half). The axis of symmetry lies vertically in the middle of each figure. The combined images are truncated and only the portions that efficiently demonstrate the wave phenomenon of interest are presented. The figures visualize the incident plane wave and the reflected/diffracted waves including center wave, wake, and edge wave. The white arrows indicate the direction of propagation for the airborne waves.

Figure 4(a) shows a plane wave propagating toward the paraboloidal reflector at $t = 250$ μs. This incident wave corresponds to the direct wave shown in Fig. 2. Figure 4(b) shows the wake and edge wave reflected from the paraboloidal reflector at $t = 550$ μs. A spherical wavefront (dashed line) is observed with its center located at the reflector edge. Since the model is axisymmetric, the edge wave would be a doughnut-shaped wavefront in a 3D space. As predicted in Fig. 2(b), the edge wave has the same phase as the incident plane wave before passing through focal point ($z > z_F$). The wake is not clearly shown in this figure given that its amplitude is relatively weak. However, wave interference on the interior reflector surface indicates the presence of wake and demonstrates the interaction between the wake and the edge wave. Figure 4(c) shows the moment before focusing occurs when all waves converge toward the focal point. The center wave has been radiated from the vertex of the reflector but can hardly be identified because of the wave interference. Figure 4(d) demonstrates a clear center wave at $t = 900$ μs with its phase opposite to the incident plane wave after passing through the focal point.

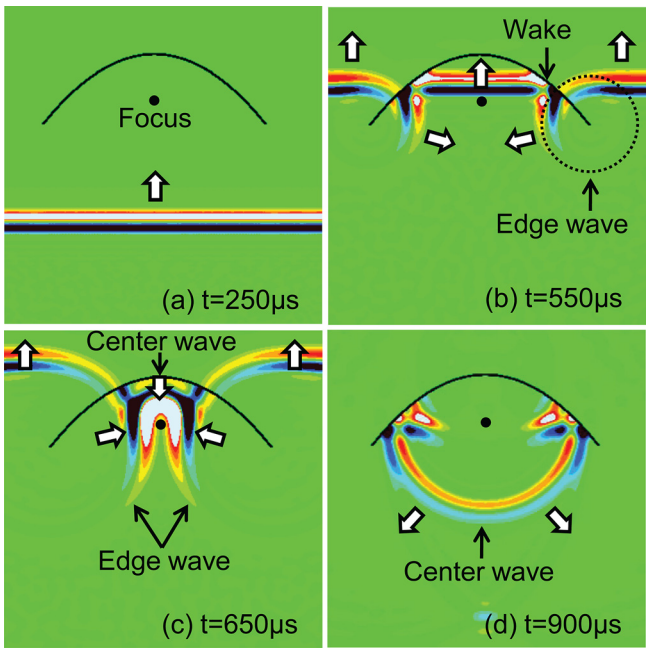

FIG. 4. (Color online) Visualization of the wave field in air at (a) $t = 250$ μs, (b) $t = 550$ μs, (c) $t = 650$ μs, and (d) $t = 900$ μs. The input plane wave has a waveform of an one-cycle sinusoid with a period of 50 μs.

2. On-axis signal comparison

Simulated signals along the reflector axis at $z = 2$, 4, 6, and 8 cm are shown in Fig. 5. These signals were obtained using both analytical and numerical models. A longer period of the sinusoidal function ($T = 150$ μs) was used to minimize energy dissipation of waves during propagation induced by meshing. Given $T = 150$ μs, the calculated ka (Ref. 17) at the center frequency of the input function is 7.85, which is sufficiently larger than one to fulfill the frequency requirement for geometrical acoustics. Signals in Fig. 5 show agreement between the analytical and FEM results for arrival times and pressure amplitudes. However, as the observation point moves further beyond the focal point ($z = 6$ cm, 8 cm), discrepancy is observed. The wave amplitudes of simulation results are smaller than that given by the analytical results. A possible explanation for this discrepancy may be mesh damping induced by the FEM model. In finite element analysis, the mesh acts like a low-pass filter and dissipates energy of propagating waves.[23] Therefore, as the waves propagate further, more energy is dissipated and the its pressure amplitude decreases accordingly, as shown in Figs. 5(c) and 5(d).

FEM simulation results presented in this section has validated the analytical solution. This axial solution captures the behavior of each wave and gives correct on-axis response. In Sec. V, this analytical solution is used to

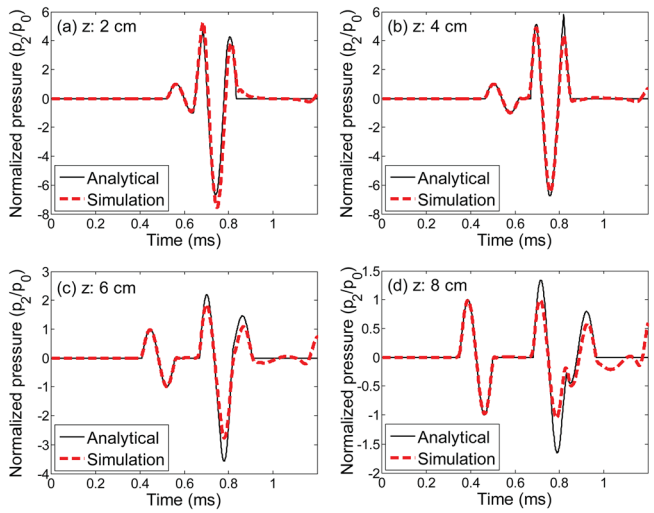

FIG. 5. (Color online) Analytical and simulation results along axis at (a) $z = 2$ cm, (b) $z = 4$ cm, (c) $z = 6$ cm, (d) $z = 8$ cm. The focal point is at $z = 3.1$ cm. The direct wave is included for reference. The disturbances in numerical results at late time are caused by reflection from the model boundary.

investigate the focusing effect provided by reflectors with various geometries. In addition, pressure responses in the focal zone is also studied.

V. INVESTIGATION OF FOCUSING EFFECT

The geometry of a paraboloidal reflector can be described by the equation $r^2 = 4z_F z$. However, this equation does not express the characteristics of a parabola intuitively. Other systems, such as the rim angle or h/z_F for a fixed reflector aperture shown in Fig. 6(a) are widely used and give an intuitive expression of the reflector dimensions. Rim angle (θ) is defined as the angle between reflector axis and the line connecting the focal point and the reflector edge. For a paraboloidal reflector with a rim angle of 90°, the focal point is located at the center of the aperture. Figure 6(b) shows nine parabolas with different rim angles from 30° to 150° with a 15° increment. In this figure, these parabolas are presented in such a way that their focal points are fixed at the point $r = z = 0$ while the depth changes. Both the rim angle θ and h/z_F are used in this paper to describe the geometries of paraboloidal reflectors, and they are related to each other by equation

$$\frac{h}{z_F} = \frac{1 - \cos\theta}{1 + \cos\theta}. \tag{13}$$

A. Dependence of focusing gain on reflector geometry

Equation (12) shows that the signal amplification (p_2/p_0) at the focal point is related to the reflector geometry and time derivative of the input function (df/dt). The effect of reflector geometry is presented in this section. For a given input function, the pressure gain at the focus is related to the reflector geometry by

$$\frac{p_2}{p_0} \propto z_F \ln(h/z_F + 1) = z_F G_1, \tag{14}$$

or in another form

$$\frac{p_2}{p_0} \propto r\sqrt{z_F/h}\ln(h/z_F + 1) = rG_2. \tag{15}$$

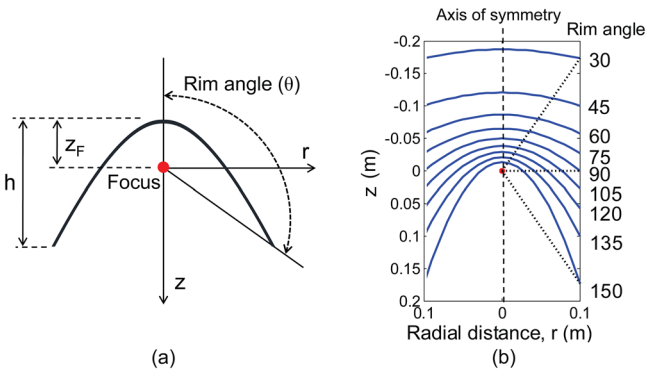

FIG. 6. (Color online) Two systems for describing geometry of a paraboloidal reflector: (a) rim angle and h/z_F with a fixed aperture radius, (b) paraboloidal reflectors with different rim angles ranging from 30° to 150°.

G_1 is the gain factor associated with paraboloidal reflectors with a fixed focal length z_F, and G_2 is the gain factor associated with paraboloidal reflectors with a fixed aperture radius r. Figure 7(a) shows the relation between G_1 and h/z_F. For paraboloidal reflectors with the same focal length z_F, increasing h/z_F indicates extension of the paraboloidal reflector in the depth direction, and the aperture area of reflector ($\pi r^2 = 4\pi z_F h$) also increases linearly with h. In this case, the aperture of the reflector increases and more sound energy is collected and focused. Based on geometrical acoustics without considering diffraction, the pressure at the focus will increase linearly with the radius r, or $\sqrt{h}$. However, Eq. (14) shows the gain factor G_1 increases with h/z_F as function $\ln(h/z_F + 1)$, when diffraction is considered.

If the radius of a paraboloidal reflector is fixed, the same amount of incident energy is considered. In this case, the pressure at the focus is affected by the geometry of reflector. Figure 7(b) shows the relation between G_2 and h/z_F. It can be seen that the maximum gain is obtained around $h/z_F = 4$. Derivation in Appendix C shows the maximum gain occurs at $h/z_F = 3.92$. This result agrees with the analysis by Wahlstrom,[13] who provided a frequency domain solution analogous to the transient solution provided here. Figure 8(a) shows the gain factor G_2 normalized by the maximum value obtained at $h/z_F = 3.92$ ($\theta = 126.4°$), and the ratio is shown as decibels. To show comparison with results by Wahlstrom,[13] the horizontal axis label h/z_F various as the power of 2. Corresponding rim angle values are also shown on the top axis. Both models give identical results and predict a maximum gain at $h/z_F \simeq 4$ or rim angle $\simeq 126.9°$. Therefore, the most efficient reflector geometry for signal amplification is determined. However, for h/z_F in the range of $1 - 16$ or rim angles from 90° to 150°, the reflectors can also be considered efficient since the gain factor drops only about 1 dB.

The variation of gain factor G_2 can be understood from the change of travel distances for the edge wave, center, and wake waves. For different reflector geometries (same aperture size), the travel distance for each type of wave from the reflector surface to the focal point is different, as shown in Fig. 6(b). For example, the waves reflected from a reflector of a rim angle of 30° need to travel longer distances to reach the focal point compared that reflected from a reflector of rim angle of 90°. Since the pressure amplitude of a reflected wave decays as it propagates (geometrical spreading), the focused pressure amplitude for 30° rim angle is smaller.

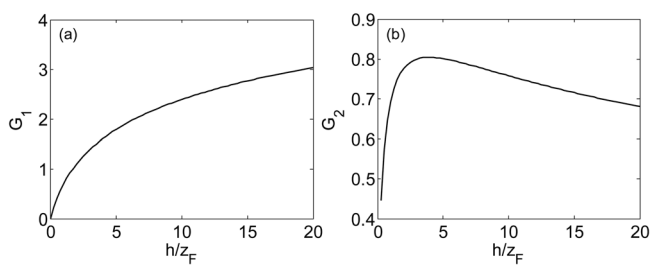

FIG. 7. Relation between gain factor and different paraboloidal reflectors with (a) a fixed focal length z_F and (b) a fixed reflector radius r.

When the rim angle reaches 120°, the focused pressure reaches the maximum.

B. Dependence of focusing gain on frequency of incident wave

The pressure amplification at focus also depends on the frequency of incident wave. By transforming Eq. (12) into frequency domain, the pressure gain can be written as

$$\frac{p_2(\omega)}{p_0} = 2jk_0 z_F \ln(h/z_F + 1)F(\omega), \tag{16}$$

where $k_0 = \omega/c_0 = 2\pi/\lambda$ is the wavenumber of the incident wave and $F(\omega)$ is the Fourier transform of $f(t)$. This equation indicates that signal amplification at the focus is linearly proportional to the frequency ω or z_F/λ of the incident wave. Figure 8(b) shows the combined effect of reflector geometry h/z_F and frequency z_F/λ on the focused signal amplification in decibels. This figure agrees with the results derived by Wahlstrom[13] based on harmonic solutions. It should be noted that, however, this conclusion is based on an assumption of $ka \gg 1$. If the requirement is not satisfied, standing wave can be formed from the interaction between the incident wave and the reflected waves,[13] which reduces the signal amplification at focus.

C. Relation between rim angle and on-axis focusing gain

On-axis signal amplification provided by paraboloidal reflectors with different rim angles is studied in this section. The investigated rim angles range from 30° to 150° with a 30° increment, and the corresponding paraboloidal reflectors shown in Fig. 6(b) are used here. The input function is a single cycle sinusoidal tone burst, and two input frequencies, 20 and 100 kHz, are used to investigate the dependence of on-axis focusing gain on the input frequency.

Figures 9(a) and 9(b) show the near-focus signal amplification along the reflector axis for different rim angles, and two input frequencies of 20 and 100 kHz, respectively. Note that the horizontal axis represents the offset distance from the focus, and ranges from −4 cm (before focus) to +4 cm (beyond focus). For a paraboloidal reflector with a large rim angle (120° a 150°, for example), because the focal point is

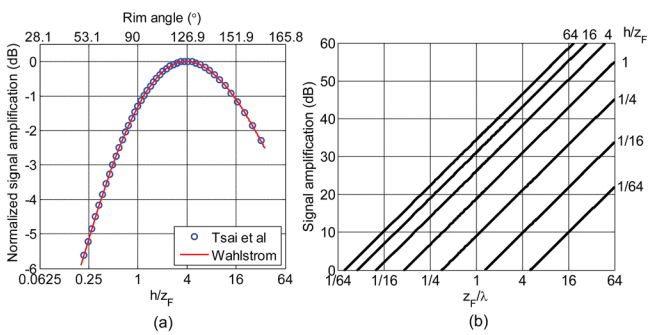

FIG. 8. (Color online) (a) Normalized signal amplification with respect to $G_{2\max}$ at $h/z_F = 3.92$, (b) signal amplification for incident waves with different frequencies (h/λ) and paraboloidal reflectors with various geometries (h/z_F).

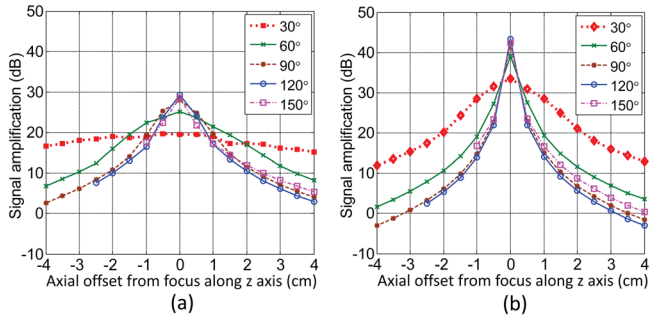

FIG. 9. (Color online) Axial signal amplification (near-focus region) given by paraboloidal reflectors with the same aperture radius 10 cm but different rim angles. Results from two input frequencies: (a) 20 kHz and (b) 100 kHz are presented. The focal point corresponds zero offset on the horizontal axis.

very close to the reflector vertex, only limited number of results can be obtained in the region between focal point and vertex.

In both figures, the signal amplification reaches the maximum at the focal point and drops elsewhere. In the near focus region, the 100 kHz wave gives higher signal amplification than the 20 kHz wave. However, the sizes of focal zone in two figures are different, and they depend on both the rim angle and the input frequency. First, a small rim angle of 30° gives a relatively flat amplification curve in both figures while a large rim angle of 120° gives a much sharper one. The focal zone narrows as the rim angle increases from 30° to 120° and then widens as the rim angle keeps increasing to 150°. This result indicates that a reflector that provides higher focusing gain has a narrower focal zone and vice versa. Second, the input frequency affects the focal zone size. The amplification curve for each rim angle in Fig. 9(b) is much sharper than the corresponding curve in Fig. 9(a). In addition, the signal amplification drops much faster in Fig. 9(b) as the observation point moves away from the focal point. This indicates that a higher input frequency has a narrower focal zone.

The variations of on-axis signal amplification (off-focus) and the focal zone size are related to the arrival times and frequencies of the reflected wave. Figure 10 shows the time domain signals obtained at 2 cm beyond focus for rim angles of 30°, 60°, 120°, and 150°. The input plane wave is a single cycle sinusoidal pulse with an input frequency of 20 kHz. For small rim angles (30° and 60°), the reflected waves arrive almost simultaneously and result in high constructive interference. The resulting waves shown in Figs. 10(a) and 10(b) are quite similar to the signal obtained at focus, and they can still be considered as focused waves but with lower amplitudes (slightly defocused). However, for large rim angles (120°and 150°), it is clear that the three reflected waves (center, edge, and wake) arrive at different times and thus there is very limited constructive interference. Therefore a small rim angle gives a wide focal zone while a large rim angle gives a narrow focal zone. Arrival times of the center wave, edge waves, and wake are related to their travel paths. As can be seen in Fig. 6(b), the distance between the reflector surface and the focal point is large for the reflector with rim angle of 30°. Therefore, a 2 cm shift from the focal point along axis introduces a relatively small

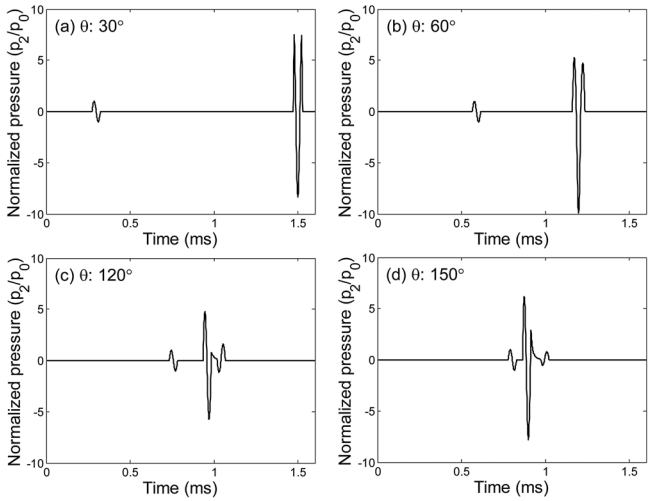

FIG. 10. Time-domain signals obtained at 2 cm beyond focal point given by rim angle of (a) 30°, (b) 60°, (c) 120°, (d) 150°.

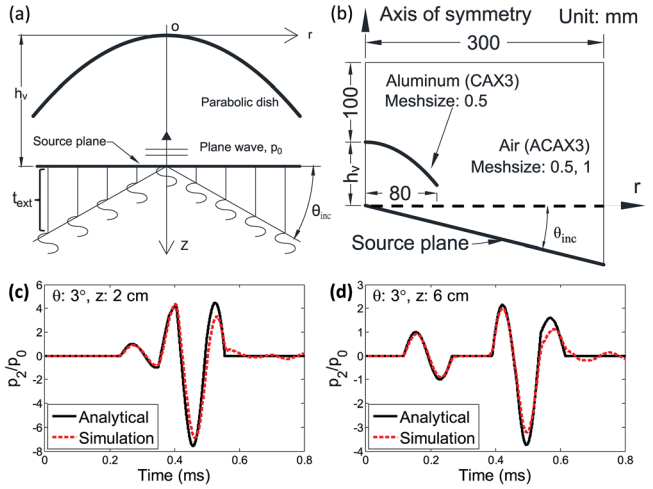

FIG. 11. (Color online) (a) Conceptual model for an incident wave with a conical shape. Extra delay times are added to the input functions to form a conical wavefront. (b) Model for FEM simulation. (c) and (d) Analytical and simulation results obtained at $z = 2$ cm and $z = 6$ cm along the axis given by conical waves with an inclined angle of 3°.

amount of extra travel distance for the center, edge, and wake waves. As a result, their travel times to focus are elongated by about the same amount and the resulting wave has a shape similar to the signal obtained at focus. For larger rim angle like 120° or 150°, the focal lengths are about 2.5 and 1.25 cm, respectively. A 2 cm shift from focal point introduces considerably amount of extra distance compared to the original travel path, therefore their arrival times are much different as shown in Figs. 10(c) and 10(d) and result in less constructive interference. A high frequency incident wave with short wavelength has less chance to build constructive interference than a low frequency wave. Therefore, a higher frequency incident wave has a narrower focal zone.

VI. INCIDENT WAVES WITH ARBITRARY AXISYMMETRICAL WAVEFRONT

The analytical solution given by Eq. (4) can be extended to incident waves with non-planar, non-uniform axisymmetric wavefront. The entire paraboloidal reflector can be divided into a finite number of rings, and each ring is assigned a specific input waveform. Given the axisymmetric model in Fig. 1, the radial distance, r, is used to describe any ring (with radius r) on the paraboloidal reflector as well as its projection (a source ring with same radius r) on the source plane. According to geometrical acoustics, the rays emitted from the source ring would be reflected solely by the corresponding ring (with the same radius r) on the reflector surface. In addition, the required arrival time for the rays to reach the observation point other than the focal point has a unique value between t_1 and t_2. As a result, each arrival time (t') in the integral of the wake term in Eq. (4) can be related exclusively to its corresponding source ring with a radius of r. With this discretization procedure, the rays emitted from the source rings with different radius r can be considered individually in the wake integral. For the edge and the center waves, the corresponding input functions can be directly included in the first two terms in Eq. (4).

An axisymmetric wavefront can be achieved by assigning different input functions along r on the source plane. Figure 11(a) shows an example for an incident conical wave. Extra delay times, t_{ext}, are included at the beginning of each input functions and are determined by the inclined angle, θ_{inc}, using the relation $t_{\text{ext}} = r\tan(\theta_{\text{inc}})$. Figure 11(b) shows the FEM model. A paraboloidal reflector with a radius of 8 cm and a depth of 5 cm is used. The focal length is 3.1 cm, and h_v is 10 cm. An one-cycle sinusoid with a period of 150 μs is specified along the inclined face as input. Figures 11(c) and 11(d) show the on-axis responses obtained at 2 and 6 cm from reflector vertex, and the inclined angles of the simulated conical wavefront is 3°. The analytical and simulation results in Fig. 11 show good agreement in the region away from the focal zone. Since the incident wave is not planar, the focal point shifts.

VII. CONCLUSIONS AND FUTURE WORK

A transient solution has been derived for the axial response of reflected plane waves from a paraboloidal reflector. This solution provides an impulse response of the system, and the response to any transient input can be obtained by convolution. Numerical simulations using FEM are performed to visualize the wave field in air and validate the analytical solution. Numerical simulations also provide a better understanding about how the reflected waves propagate and interfere with each other.

The analytical solution shows that the axial response consists of three components: The center wave, edge wave, and wake. These three waves are generated from the reflector's center, edge, and entire surface, respectively, and their arrival times, amplitudes, and phases vary with the location of the observation point. For incident plane waves, all waves arrive at the focal point of the reflector at the same time, therefore their constructive interference is maximized. The resulting focused wave has a waveform of the time-derivative of the input function and has the maximum pressure amplitude on the axis.

Dependence of focusing gain on reflector geometry and input frequency was studied. For a fixed input frequency, the focusing gain reaches maximum when the rim angle $\simeq 126.4^\circ$ ($h/z_F = 3.92$). For high frequency waves satisfying the requirement of $ka \gg 1$, the focused pressure amplitude varies linearly with the input frequency. As a result, plotting the focusing gain against reflector geometry and input frequency in decibels results in a family of straight lines parallel to each other as shown in Fig. 8(b). Reflector geometry and input frequency also affect the size of focal zone. The size of focal zone is wider for smaller rim angle or lower input frequency, and becomes sharper as the rim angle approaches 126.4° or with higher input frequency. Trade-off between the focusing gain and the size of focal zone is presented and can serve as a guideline for selecting appropriate paraboloidal reflector.

The analytical solution is extended to analysis of incident waves with axisymmetric wavefronts by using a discretization procedure. An example of an incident conical wave is presented and the analytical and simulation results agree well in the region away from focal point. Since the incident wave is not planar, focal shift occurs and the phase reversal behavior of each reflected wave in the near-focus region is different. Behavior of phase reversal for an incident wave with arbitrary wavefront will be studied in the future. The discretized solution also allows a non-uniform pressure distribution of the incident wave. This analytical solution will be generalized to account for incident waves with any axisymmetric wavefront and pressure distribution in the future.

ACKNOWLEDGMENTS

The authors thank Professor Mark F. Hamilton for his valuable comments and suggestions during the manuscript preparation. This work was supported by NIST Technology Innovation Program (TIP).

APPENDIX A: DERIVATION OF ON-AXIS SOLUTION

The following derivation of the transient on-axis pressure field reflected by a paraboloidal reflector follows the procedure used by Hamilton[14] for obtaining the on-axis solution resulting from a point source located at the near focus of an ellipsoidal reflector. Before evaluating the on-axis response from a paraboloidal reflector, we note that the pressure on the reflector surface p_{2g} based on the geometrical acoustics [Eq. (2)] can be represented by a convolution of the impulse response function, h_{2g}, and any arbitrary transient input function $f(t)$ as $p_{2g}/p_0 = f(t) * h_{2g}$, where

$$h_{2g} = \frac{D(z_s)}{r_2}\delta\left(t - \frac{h_v + z_F - r_2}{c_0}\right), \text{and} \tag{A1}$$

$$D(z_s) \equiv r_F = z_s + z_F. \tag{A2}$$

The function h_{2g} is found by simply setting the function $f(t)$ in Eq. (2) to the delta function, $\delta(t)$. The term $D(z_s)$ defined on the left-hand side of the above expression is the paraboloidal analog to the directivity factor used by Hamilton for ellipsoidal reflectors. It is introduced to simplify the determination of the Q factor [Eq. (A15)] used in finding the contributions by the center, edge, and wake to the field on-axis.

Using this expression, the Kirchhoff-Helmholtz integral shown in Eq. (3) now be represented by the impulse response h_2 as $p_2/p_0 = f(t) * h_2$, where

$$h_2 = \frac{1}{4\pi}\int\int_S \left\{[h_{2g}]\frac{\partial}{\partial n}\left(\frac{1}{R}\right) - \frac{1}{c_0 R}\frac{\partial R}{\partial n}\left[\frac{\partial h_{2g}}{\partial t}\right] - \frac{1}{R}\left[\frac{\partial h_{2g}}{\partial n}\right]\right\} ds. \tag{A3}$$

To evaluate h_2, each of the terms within the integral must be evaluated in terms of the paraboloidal geometry. We begin with the normal derivative of R on the reflecting surface,

$$\frac{\partial R}{\partial n} = \frac{\vec{R}\cdot\vec{e}_n}{R}, \tag{A4}$$

where R is the distance between any point on the reflector surface and the observation point on the z axis, and $\vec{R}$ is its vector form pointing from the on-axis observation point to the reflector surface. $\vec{e}_n$ is a unit vector pointing to the inward normal direction of the reflector surface ($\vec{n}$). $\vec{R}$ is thus defined by

$$\vec{R} = (z_s - z)\vec{e}_z + r\vec{e}_r. \tag{A5}$$

The equation of the reflector surface (C) can be written as

$$C(r, z_s) = r^2 - 4z_F z_s = 0, \tag{A6}$$

and $\vec{e}_n$ is therefore given by

$$\vec{e}_n = \frac{-\nabla_s \cdot C}{|\nabla_s C|} = \frac{-\sqrt{z_s/z_F}\vec{e}_r + \vec{e}_z}{\sqrt{z_s/z_F + 1}}, \tag{A7}$$

where ∇_s is the gradient evaluated on the surface of the reflector. Substituting the above terms into Eq. (A4), one obtains the following simple relationship for $\partial R/\partial n$;

$$\frac{\partial R}{\partial n} = \frac{-(z + z_s)}{R\sqrt{z_s/z_F + 1}}.$$

Using these expressions, the first term in the integrand of h_2 [Eq. (A3)] can now be determined. The notation $\{\}_s$ indicates that the terms within the brackets are evaluated on the reflector surface, which implies, for example, that r_2 be replaced with r_F within the integrand. As a result,

$$\left\{[h_{2g}]\frac{\partial}{\partial n}\left(\frac{1}{R}\right)\right\}_S = -\left\{\frac{[h_{2g}]}{R^2}\frac{\partial R}{\partial n}\right\}_S = \frac{D(z_s)(z + z_s)}{R^3 r_F\sqrt{z_s/z_F + 1}}\delta(\tau), \tag{A8}$$

where τ is the retarded time, which is defined as

$$\tau = t - \frac{h_v - z_s + R}{c_0}. \tag{A9}$$

Similarly, the second term in the integrand of Eq. (A3) becomes

$$-\left\{\frac{1}{c_0 R}\frac{\partial R}{\partial n}\left[\frac{\partial h_{2g}}{\partial t}\right]\right\}_S = \frac{D(z_s)(z+z_s)}{c_0 R^2 r_F\sqrt{z_s/z_F+1}}\frac{\partial\delta(\tau)}{\partial\tau}, \tag{A10}$$

and the last term is

$$-\left\{\frac{1}{R}\left[\frac{\partial h_{2g}}{\partial n}\right]\right\}_S = \frac{D(z_s)}{r_f R\sqrt{z_s/z_F+1}}\left[\frac{\partial\delta(\tau)/\partial\tau}{c_0} - \frac{\delta(\tau)}{r_F}\right]. \tag{A11}$$

Note that the surface area of the paraboloidal reflector (ds) in the integral can be represented with dz_s as

$$ds = 4\pi z_F\sqrt{1+z_s/z_F}dz_s. \tag{A12}$$

Employing all the above expressions, h_2 can finally be written as an integration along z_s as

$$h_2 = z_F\int_0^h\left[\left(\frac{z+z_s}{R^2} - \frac{1}{r_F}\right)\delta(\tau) + \left(\frac{z+z_s}{c_0 R} + \frac{1}{c_0}\right)\frac{\partial\delta(\tau)}{\partial\tau}\right]\frac{D(z_s)}{Rr_f}dz_s. \tag{A13}$$

The integrand in Eq. (A13) can be written as a form of integration by parts as $d[Q(z_s)\delta(\tau)]/dz_s$ by carefully choosing the function Q. Analysis shows that the Q function can be defined using the second term in Eq. (A13) as

$$\frac{1}{Rr_f}\left(\frac{z+z_s}{c_0 R} + \frac{1}{c_0}\right)\frac{\partial\delta(\tau)}{\partial\tau} \equiv Q\frac{\partial\delta(\tau)}{\partial\tau}\frac{\partial\tau}{\partial z_s}, \tag{A14}$$

which results in

$$Q = \frac{z+z_s+R}{Rr_f K}, \text{and} \tag{A15}$$

$$K = R + z - z_s - 2z_F = R + z - z_F - r_F. \tag{A16}$$

One then notes that the spatial derivative of Q with respect to the z coordinate on the surface is found as

$$\frac{\partial Q}{\partial z_s} = \left(\frac{z+z_s}{R^2} - \frac{1}{r_F}\right)\frac{1}{Rr_f}, \tag{A17}$$

which allows Eq. (A13) to be rewritten as

$$h_2 = z_F\int_0^h D(z_s)\frac{d}{dz_s}[Q(z_s)\delta(\tau)]dz_s. \tag{A18}$$

Equation (A18) can then be integrated by parts to yield the following function for h_2;

$$h_2 = z_F D(h)Q(h)\delta(\tau_e) - z_F D(0)Q(0)\delta(\tau_c) - z_F\int_0^h D'(z_s)Q(z_s)\delta(\tau)dz_s. \tag{A19}$$

The delta function in Eq. (A19) is given by

$$\delta[\tau(z_s)] = \frac{\delta(z_s - z_r)}{|\tau'(z_r)|}, \tag{A20}$$

where $\tau' \equiv \partial\tau/\partial z_s$ and z_r is the root of $\tau(z_r) = 0$. Now one notes that τ' is

$$\frac{\partial\tau}{\partial z_s} = \frac{1}{c_0}\left(1 - \frac{\partial R}{\partial z_s}\right), \tag{A21}$$

and that $R^2 = 4z_F z_s + (z - z_s)^2$, $\partial\tau/\partial z_s$ can thus be written as

$$\frac{\partial\tau}{\partial z_s} = \frac{R + z - z_F - r_F}{Rc_0} = \frac{K}{Rc_0}. \tag{A22}$$

K is a function of z and z_s. According to the reflector geometry shown in Fig. 1, K is positive for an observation point located beyond the focus $(z > z_F)$ and negative for a point located before the focus $(z < z_F)$. The delta function is therefore

$$\delta(\tau) = \frac{R_r c_0 \text{sgn}(K_r)}{K_r}\delta(z_s - z_r), \tag{A23}$$

with z_r given by

$$z_r = \frac{(tc_0 - h_v)^2 - z^2}{4z_F - 2(tc_0 - h_v + z)}. \tag{A24}$$

Substituting $\delta(\tau)$ into Eq. (A19), h_2 can be rewritten in the compact form

$$h_2 = \frac{z_F(z+h+R_e)}{R_e K_e}\delta(\tau_e) - \frac{z_F(z+R_c)}{R_c K_c}\delta(\tau_c) - \frac{z_F c_0(z+z_r+R_r)\text{sgn}(K_r)}{(z_r+z_F)K_r^2} \equiv H_e(z)\delta(\tau_e) + H_c(z)\delta(\tau_c) + H_w(z,t). \tag{A25}$$

The subscripts e, c, r indicate that the functions R and K will be evaluated at the edge $(z_s = h)$, center $(z_s = 0)$, and on the surface $(z_s = z_r)$. As a result, p_2 can be calculated from three terms representing the edge, center, and wake contributions, respectively:

$$\frac{p_2}{p_0} = f(t) * h_2(z,t) = H_e(z)f(\tau_e) + H_c(z)f(\tau_c) + \int_{t_1}^{t_2} H_w(z,t')f(t-t')dt'. \tag{A26}$$

In the above expression, t_1 and t_2 are the temporal limits of the wake defined by Eq. (A27) or Eq. (A28) depending on the z coordinate of the observation point. For $z < z_F$, the

leading contribution of the wake arrives from the reflector center while the contribution arriving from reflector edge arrives last. In that case, t_1 and t_2 are written as

$$t_1 = \frac{h_v + z}{c_0} \quad \text{and} \quad t_2 = \frac{h_v - h + R_e}{c_0}. \tag{A27}$$

On the contrary, for $z > z_F$,

$$t_1 = \frac{h_v - h + R_e}{c_0} \quad \text{and} \quad t_2 = \frac{h_v + z}{c_0}. \tag{A28}$$

Note that a singularity occurs when the observation is located at the geometric focus. A special solution for pressure response at focal point is given in Appendix B.

APPENDIX B: SOLUTION AT GEOMETRIC FOCUS

The solution for axial response given in Appendix A has a singularity when the observation point coincides with the focal point. A special solution is therefore presented here for that special point of interest. By setting $z = z_F$, Eq. (A13) can be written as

$$h_2 = \frac{2z_F}{c_0}\frac{\partial\delta(\tau)}{\partial\tau}\int_0^h \frac{1}{r_F}dz_s = \frac{2z_F\ln(h/z_F+1)}{c_0}\frac{\partial\delta(\tau)}{\partial\tau}. \tag{B1}$$

Then, since $\partial\tau/\partial t = 1$ in this case, and the chain rule yields

$$\frac{\partial\delta(\tau)}{\partial\tau} = \frac{\partial\delta(\tau)}{\partial\tau}\frac{\partial\tau}{\partial t} = \frac{\partial\delta(\tau)}{\partial t},$$

the expression for h_2 simplifies to

$$h_2 = \frac{2z_F\ln(h/z_F+1)}{c_0}\frac{\partial\delta(\tau)}{\partial t}, \tag{B2}$$

and thus the pressure at any on-axis observation point is given in the following compact form

$$\frac{p_2}{p_0} = h_2 * f(t) \tag{B3}$$

$$= \frac{2z_F\ln(h/z_F+1)}{c_0}\frac{d}{dt}f\left(t - \frac{h+z_F}{c_0}\right). \tag{B4}$$

APPENDIX C: CRITICAL VALUE OF G_2 FOR MAXIMUM SIGNAL AMPLIFICATION

To investigate the influence of reflector geometry on gain at the reflector focus, Sec. V A introduced a gain factor, G_2 given in Eq. (15). By replacing h/z_F with x, in that expression, one has

$$G_2 = \sqrt{1/x}\ln(x+1), \tag{C1}$$

an expression that can then be used to determine the value of h/z_F that maximized the focusing gain for a given input function. This is done by setting $\partial G_2/\partial x$ equal to zero,

$$\frac{\partial G_2}{\partial x} = \frac{\sqrt{x}/(x+1) - \ln(x+1)/2\sqrt{x}}{x} = 0, \tag{C2}$$

and finding the root. The above equation can be simplified as

$$\frac{2x}{x+1} = \ln(x+1). \tag{C3}$$

Equation (C3) does not have an analytical solution, but numerical root finding shows that a maximum for G_2 occurs when $x = h/z_F \simeq 3.92$, which corresponds to a rim angle of $\simeq 126.4^\circ$.

[1]S. D. Holland, S. V. Teles, and D. E. Chimenti, "Air-coupled, focused ultrasonic dispersion spectrum reconstruction in plates," J. Acoust. Soc. Am. **115**, 2866–2872 (2004).
[2]X. Dai, J. Zhu, Y.-T. Tsai, and M. R. Haberman, "Use of parabolic reflector to amplify in-air signals generated during impact-echo testing," J. Acoust. Soc. Am. **130**, EL167–EL172 (2011).
[3]S. D. Holland and D. E. Chimenti, "Air-coupled acoustic imaging with zero-group-velocity Lamb modes," Appl. Phys. Lett. **83**, 2704–2706 (2003).
[4]A. Gibson and J. Popovics, "Lamb wave basis for impact-echo method analysis," J. Eng. Mech. **131**, 438–443 (2005).
[5]J. Zhu and J. Popovics, "Imaging concrete structures using air-coupled impact-echo," J. Eng. Mech. **133**, 628–640 (2007).
[6]S.-H. Kee, T. Oh, J. S. Popovics, R. W. Arndt, and J. Zhu, "Nondestructive bridge deck testing with air-coupled impact-echo and infrared thermography," J. Bridge Eng. **17**, 928–939 (2012).
[7]Y.-T. Tsai and J. Zhu, "Simulation and experiments of airborne zero-group-velocity Lamb waves in concrete plate," J. Nondestruct. Eval. **31**, 373–382 (2012).
[8]H. F. Olson and I. Wolff, "Sound concentrator for microphones," J. Acoust. Soc. Am. **1**, 410–417 (1930).
[9]O. B. Hanson, "Microphone technique in radio broadcasting," J. Acoust. Soc. Am. **3**, 81–93 (1931).
[10]R. C. Coile, "The parabolic sound concentrator," J. Acoust. Soc. Am. **11**, 167 (1939).
[11]R. S. Little, "Acoustic properties of parabolic reflectors," J. Acoust. Soc. Am. **40**, 919–920 (1966).
[12]S. Wahlstrom, "The parabolic reflector as an acoustical amplifier," J. Audio Eng. Soc. **33**, 418–429 (1985).
[13]E. P. Cornet and D. T. Blackstock, "Focusing of an N wave by a spherical mirror," J. Acoust. Soc. Am. **52**, 115 (1972).
[14]M. F. Hamilton, "Transient axial solution for the reflection of a spherical wave from a concave ellipsoidal mirror," J. Acoust. Soc. Am. **93**, 1256–1266 (1993).
[15]M. F. Hamilton, "Transient axial solution for the reflection of a spherical wave from a paraboloidal mirror," J. Acoust. Soc. Am. **96**, 3225–3226 (1994).
[16]L. J. Gelin, J. M. Shorey, D. M. Hester, and D. T. Blackstock, "Experimental study of reflection of airborne, spark-produced N waves by a paraboloidal dish," J. Acoust. Soc. Am. **96**, 3226 (1994).
[17]D. T. Blackstock and C. L. Morfey, "Reflection and transmission of spherical waves incident on a concentric spherical interface," J. Acoust. Soc. Am. **89**, 1971 (1991).
[18]D. Blackstock, *Fundamentals of Physical Acoustics* (Wiley-Interscience, Hoboken, NJ, 2000), pp. 472–476.
[19]J. N. Tjotta and S. Tjotta, "Nearfield and farfield of pulsed acoustic radiators," J. Acoust. Soc. Am. **71**, 824–834 (1982).
[20]T. J. R. Hughes, *The Finite Element Method: Linear Static and Dynamic Finite Element Analysis* (Dover, Mineola, NY, 2000), pp. 493–495.
[21]Y.-C. Wang, V. Murti, and S. Valliappan, "Assessment of the accuracy of the Newmark method in transient analysis of wave propagation problems," Earthquake Eng. Struct. Dyn. **21**, 987–1004 (1992).
[22]D. Alleyne and P. Cawley, "A two-dimensional Fourier transform method for the measurement of propagating multimode signals," J. Acoust. Soc. Am. **89**, 1159–1168 (1991).
[23]D. W. Zingg, H. Lomax, and H. Jurgens, "High-accuracy finite-difference schemes for linear wave propagation," SIAM J. Sci. Comput. **17**, 328–346 (1996).